CHEMISTRY OF MATERIALS

Article

pubs.acs.org/cm

Investigating the Intercalation Chemistry of Alkali Ions in Fluoride Perovskites

Tanghong Yi,[†,‡] Wei Chen,[‡,¶] Lei Cheng,[‡,§] Ryan D. Bayliss,[†] Feng Lin,[‡,∥] Michael R. Plews,[†] Dennis Nordlund,[⊥] Marca M. Doeff,[‡] Kristin A. Persson,[‡] and Jordi Cabana*[,†]

[†]Department of Chemistry, University of Illinois at Chicago, Chicago, Illinois 60607, United States

[‡]Energy Storage and Distributed Resources Division, Lawrence Berkeley National Laboratory, Berkeley, California 94720, United States

[§]Department of Materials Science and Engineering, University of California Berkeley, Berkeley, California 94720, United States

[⊥]SLAC National Accelerator Laboratory, 2575 Sand Hill Road MS69, Menlo Park, California 94025, United States

[¶]Department of Mechanical, Materials, and Aerospace Engineering, Illinois Institute of Technology, Chicago, Illinois 60616, United States

Supporting Information

ABSTRACT: Reversible intercalation reactions provide the basis for modern battery electrodes. Despite decades of exploration of electrode materials, the potential for materials in the nonoxide chemical space with regards to intercalation chemistry is vast and rather untested. Transition metal fluorides stand out as an obvious target. To this end, we report herein a new family of iron fluoride-based perovskite cathode materials $A_xK_{1-x}FeF_3$ (A = Li, Na). By starting with $KFeF_3$, approximately 75% of K^+ ions were subsequently replaced by Li^+ and Na^+ through electrochemical means. X-ray diffraction and Fe X-ray absorption spectroscopy confirmed the existence of intercalation of alkali metal ions in the perovskite structure, which is associated with the $Fe^{2+/3+}$ redox couple. A computational study by density functional theory showed agreement with the structural and electrochemical data obtained experimentally, which suggested the possibility of fluoride-based materials as potential intercalation electrodes. This study increases our understanding of the intercalation chemistry of ternary fluorides, which could inform efforts toward the exploration of new electrode materials.

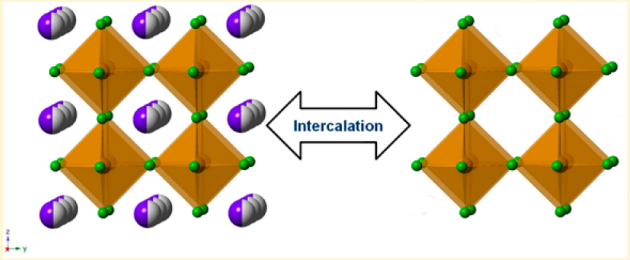

INTRODUCTION

The study of the intercalation chemistry of alkali ions in transition metal-containing hosts has fascinated scientists for the past 40 years. The ability to intercalate large amounts of lithium enabled the advent of modern Li-ion batteries. It is also at the core of many efforts to develop next-generation energy storage solutions to enable the integration of renewable energy sources for a modern sustainable society. With major challenges arising from the difficulties in achieving high energy density and extended life at a reasonable cost, new battery chemistries for electric vehicles and smart grids applications are a field of intensive research.[1] Searching for new electrode materials to replace the oxide cathodes used currently in Li-ion technologies is the fastest way toward leaps in storage capability. The underlying reason is that current cathodes possess about half of the reversible specific capacity of the commercial graphite anodes and, as a result, are the limiting components.

The chemistry of fluoride-containing compounds has been of historic interest due to the highly electronegative nature of the ion. The highly ionic nature of the transition metal-fluoride bonds elevates the redox potential of the material and renders fluorides interesting in the search for an intercalation cathode that enables devices with high energy density. It is also of interest that these highly electronegative species might be able to stabilize highly oxidized transition metals upon high rate cycling, which would lead to better safety through the reduced likelihood of material degradation. Among the redox-active transition metals, iron is particularly attractive due to its abundance, cost, and environmentally benign nature. Prior to this report, a few binary iron fluoride phases (FeF_3, FeF_2, and $FeF_3{\cdot}xH_2O$)[2−7] and mixed-anion compounds (FeOF)[8−10] have been studied as active materials for electrochemical energy storage.[2,5,11−15] However, most of these phases were found to react through conversion mechanisms, where the fluoride compounds are reduced all the way to metallic particles and LiF. This mechanism results in severe capacity losses during cycling.[16] To incorporate Li into the cathode, as required to pair it with Li-free graphite anodes, a nanocomposite of FeF_2 and LiF has been investigated.[3] This nanocomposite also shows a very complex transformation mechanism with the hypothe-

Received: October 5, 2016
Revised: January 19, 2017
Published: January 20, 2017

DOI: 10.1021/acs.chemmater.6b04181
Chem. Mater. 2017, 29, 1561−1568

sized existence of intermediate ternary phases of poor crystallinity. The outcome was still a deficient ability to cycle reversibly.

Topotactic intercalation mechanisms, where atomic arrangements are not severely disrupted, continue to be preferred in the design of new cathode materials.[17] Aside from the small solubility of Li in FeF_3 (to roughly $Li_{0.5}FeF_3$) before conversion, only Li_3FeF_6 and $LiFe_2F_6$ were clearly shown to possess electrochemical activity through intercalation mechanisms.[18−20] Other iron based fluorides such as $LiNiFeF_6$[21] and Na_3FeF_6[22] have been experimentally synthesized and studied, but their electrochemical properties were rather poor. Most of these ternary phases contain Fe (III),[23,24] which is difficult to oxidize further during the initial lithium deintercalation (cell charge). No reports were found of the electrochemical properties of Li−Fe(II)−F phases, although some of the ternaries, such as $LiFeF_3$ and Li_2FeF_4,[25] have been predicted to exist by first-principles calculations. In contrast, ternary phase Fe(II) fluorides with other alkali metals are known such as K_2FeF_4, $KFeF_3$, and $NaFeF_3$.[26−28] $KFeF_3$ has a cubic perovskite (ABX_3) structure (space group $Pm\bar{3}m$), where Fe ions sit at the B-site, six-fold coordinated with F ions, and K ions reside in the A-site, 12-fold coordinated with F ions. The idealized cubic perovskite structure is expected to exist within certain values of the tolerance factor, $t = (r_A + r_O)/\sqrt{2}(r_B + r_O)$, where r_A, r_B, and r_O are ionic radii for A, B, and O, respectively.[29] When t is lower than 0.75, the perovskite structure will tend to deviate from the ideal cubic form while attempting to reduce bonding strain.[29,30] The tolerance factors for $KFeF_3$, $NaFeF_3$, and $LiFeF_3$ (where r_F is substituted for r_O in the equation above) are around 0.91, 0.79, and 0.70, respectively, assuming they all retain the perovskite structure. In fact, $NaFeF_3$ has been shown to distort to an orthorhombic symmetry structure.[28,31] Likewise, $LiFeF_3$ would be expected to exist in a lower symmetry system if it can be made.

Perovskites constitute a family of materials that exhibit many interesting properties and are widely used in modern chemical industry as catalysts,[29] solid oxide fuel cell components,[32−35] solar cells[36] and phosphors,[37] among many other applications. Recently, there have been extensive studies on perovskites as solid electrolytes for Li-ion batteries due to their fast ionic conduction and as electrocatalysts for Li−O_2 batteries and regenerative fuel cells.[38−40] However, very limited studies on perovskites as battery electrode materials have been reported,[41] despite the intrinsic high diffusion rate of ions in many perovskite phases. Since $LiFeF_3$, if existent, is unlikely to crystallize in the perovskite structure because of the small ionic radius of Li^+ (76 pm) with respect to the A cavity, we explored perovskite structures with Fe^{2+} and mixed K/alkali metal (Li or Na) contents, $A_xK_{1-x}FeF_3$ (A = Li, Na). This outcome was achieved by electrochemically replacing the large alkali ion with smaller Li or Na. Herein, we report the synthesis, electrochemical behavior, and physical characterization of the compounds. The resulting phases showed reversible intercalation chemistry leveraging the Fe^{2+}/Fe^{3+} redox couple.

EXPERIMENTAL METHODS

$KFeF_3$ was synthesized through conventional solid-state chemistry method. In the solid-state method, KF (powder, Sigma-Aldrich, ≥ 99.99%) and FeF_2 (powder, Sigma-Aldrich) were used as starting materials. They were mixed in stoichiometric ratios in a tungsten carbide jar on a SPEX SamplePrep 8000 M mixer/mill for 30 min. The mixture was pressed into pellets, placed in Pt crucibles, and annealed at 500 °C for 12 h under Ar gas flow.

Electrochemical experiments were conducted in two-electrode 2032 coin-type cells. Lithium or sodium metal was used as both the counter and pseudoreference electrode, and a solution of either 1 M $LiPF_6$ or $NaPF_6$ dissolved in 1:1 volume mixture of ethylene carbonate (EC)/dimethyl carbonate (DMC) was used as the electrolytic solution. The solution for Na cells was made in-house, while that for the lithium cells was purchased from Novolyte. Cells were assembled in an argon-filled glovebox. Electrochemical measurements were conducted using a VMP3 potentiostat at room temperature. Galvanostatic cycling was conducted at a current rate of C/30, where C was defined as 223 and 197 mAh/g for Li ($LiFeF_3$) and Na ($NaFeF_3$) cells, respectively (theoretical capacities of $LiFeF_3$ and $NaFeF_3$, respectively). However, the capacities of $A_xK_{1-x}FeF_3$ (A = Li, Na) compounds in this paper were calculated based on the weight of $KFeF_3$, which was the starting material in the electrodes contained in the cells. Composite electrodes were prepared by mixing $KFeF_3$ and carbon black in a 6 wt % polyvinylidene difluoride (PVDF) solution in 1-methyl-2-pyrrolidone (NMP), to reach an active material/binder/carbon weight ratio of 45:45:10. $KFeF_3$ and carbon black were premixed in a planetary ball mill (Retsch PM 100) at 500 rpm for 12 h. The slurry was mixed until homogeneity was reached and was subsequently cast onto Al foil using a doctor blade. All the electrode processing was done inside an argon filled glovebox. The electrodes were left to dry under ambient temperature in the glovebox overnight before being placed in a vacuum oven at 110 °C for 12 h.

The composition and crystallinity of the $KFeF_3$ samples were evaluated by powder X-ray diffraction (XRD). Patterns were collected between 10° and 80°, 2θ, at a rate of 0.02°/min using a Bruker D2 phaser diffractometer using Cu Kα radiation (λ = 1.5418 Å). Operando synchrotron XRD data were collected on beamline 11−3 at the Stanford Synchrotron Radiation Lightsource (SSRL, Menlo Park, CA) with a Si (311) crystal monochromator. Data were collected continuously in 3 min acquisitions on the coin cell in transmission geometry during cycling. A special 2032 coin-type cell was made with a hole in the center of the spacer, bottom, and top coin cell parts for the beam path.[42] The coin-type cell was subsequently sealed in a pouch with two leads to connect the electrodes to the cycler. The stage was rocked by 0.02 mm during beam exposure to minimize beam damage. Both LaB_6 and the current collector Al were used as external and internal standards, respectively.

The particle sizes and morphologies of samples were analyzed using scanning electron microscopy (SEM). Micrographs were collected on a JEOL 7500F microscope operated at 15 kV and 20 mA in SEM mode, and the elemental distribution of samples was examined with an energy dispersive X-ray spectroscopy (EDS) detector (Thermo-Fisher). The electrodes for EDS were recovered from cycled coin cells and washed with DMC in an argon-filled glovebox.

Soft X-ray absorption spectroscopy (XAS) measurements were carried out on the 33-pole wiggler beamline 10−1 at the Stanford Synchrotron Radiation Lightsource (SSRL, Menlo Park, CA) using a ring current of 350 mA and a 1000 × 1 mm^{-1} spherical grating monochromator with 20 μm entrance and exit slits. Data were obtained at a spectral resolution of ∼0.2 eV in fluorescence yield (FY) mode to acquire bulk information on the material. The angle of incidence in FY mode was selected so as to minimize self-absorption while still being bulk sensitive. The beam footprint on the sample was 1 mm^2. Samples were attached to a bar-shape aluminum sample holder using conductive carbon tape. All samples for soft XAS study were $KFeF_3$ pristine and that cycled versus Li at different state of charge (D1 V, D2 V, C4.5 V).

Fe K-edge XAS transmission spectra were collected on $KFeF_3$ samples at different states of charge or discharge at beamline 20-BM-B at the Advanced Photon Source (APS), in transmission mode using a Si (111) double crystal monochromator. A Fe metal standard foil, located in front of a reference ion-chamber for the Fe edge, was measured simultaneously with each spectral sample for energy calibration. All data processing, including normalization, was carried out using the software SIXPACK by fitting a linear polynomial to the

DOI: 10.1021/acs.chemmater.6b04181
Chem. Mater. 2017, 29, 1561−1568

pre-edge region and a quadratic polynomial to the postedge region of the absorption spectrum. The energy threshold E_0 of the reference Fe foil was determined from the first derivative peak of the spectrum, and all XANES spectra were linearly calibrated using the difference between the obtained E_0 and the tabulated absorption edge energy for Fe K-edge. Pre-edge background subtraction and XANES normalization were carried out. Background removal and edge-step normalization were performed using Demeter program pack with Athena. IFEFFIT was then used to fit the EXAFS by Artemis in the Demeter software package.[43] The fitting was limited to a k range of 2−10 Å^{-1}, dk = 1 Å^{-1} using Hanning windows, R range from 1−4 Å. The pristine sample was designated $KFeF_3$ pristine, and samples C4.5 V, D2 V were $KFeF_3$ cycled versus Li, and Na_1.9 V was cycled versus Na. FeF_2 and FeF_3 are commercial products used as references.

Total energy calculations based on density functional theory (DFT) were performed to understand the phase stability of perovskite $Li_xK_{1-x}FeF_3$ and $Na_xK_{1-x}FeF_3$ structures. The relaxed perovskite $KFeF_3$ structure from the Materials Project was used as the original perovskite framework, whose K sites were replaced with Li (or Na) completely or partially (in supercells) to model distinct K−Li (or K−Na) orderings at different compositions.[25] The structure enumeration procedure was commonly employed in combination with the cluster expansion formalism to identify low energy structures for a lattice system.[44−46] We calculated 54 structures for $Li_xK_{1-x}FeF_3$ and 41 structures for $Na_xK_{1-x}FeF_3$. The DFT calculations used the project augmented wave (PAW) method[47] as implemented in the Vienna ab initio Simulation Package (VASP)[48] with a plane-wave energy cutoff of 520 eV. The generalized gradient approximation (GGA) of Perdew−Burke−Ernzerhof (PBE)[49] was used to approximate the electronic exchange and correlation energy. GGA+U calculations with U parameters consistent with the Materials Project were performed for the fluorides.[50] The Brillouin-zone integration was sampled with a Monkhorst−Pack mesh of 1000 k-points per atom. Spin polarization was considered with a high spin ferromagnetic initialization. All structures were allowed to fully relax and the total energy was converged within 5 meV per atom. XRD simulations of $KFeF_3$, $K_{0.5}FeF_3$, and $Li_{0.5}K_{0.5}FeF_3$ were performed with PowderCell software.[51] For the XRD simulations, the same crystal structure and lattice cell parameters were used, and only the site occupancy was changed for three compounds in the simulation to compare the reflection intensity change on varying the A site element.

RESULTS AND DISCUSSION

$KFeF_3$ was obtained through a solid state route. The XRD pattern (Figure 1a) matched $KFeF_3$ with a cubic perovskite

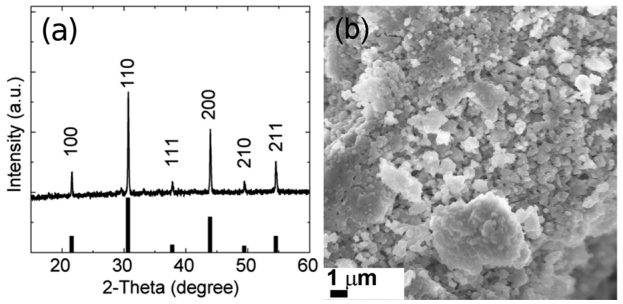

Figure 1. (a) XRD patterns of $KFeF_3$ compared with reference (PDF#200895), (b) SEM image of $KFeF_3$.

structure (PDF# 200895) showing high crystallinity. One small additional reflection that could not be accounted by $KFeF_3$ appeared around 30°, 2θ, which was possibly due to a K_2FeF_4 impurity. The intensity indicates that any impurity was present at a very low concentration, and thus, it did not affect the conclusions on $KFeF_3$ presented hereafter. The morphology and particle size distribution were investigated with SEM (Figure 1b). The particle size of $KFeF_3$ was around 1 μm, as expected from the high temperature calcination routes, with both cubic and spherical particle morphologies (Figure 1b).

To evaluate the ability of $KFeF_3$ to undergo a redox intercalation reaction, the compound was used as the working electrode in a coin cell with an alkali metal (Li or Na) as counter electrode. In the first step, $KFeF_3$ was driven to anodic (i.e., high) potentials by charging the cell galvanostatically. This step resulted in a relatively steady increase of the cell potentials, which tended to stabilize above 4 V versus Li^+/Li^0 and 3.8 V versus Na^+/Na^0, respectively. The total accumulated charge after this anodic scan at constant current was roughly 150−170 mAh/g, equivalent to the removal of around 80% of K^+ from the compound. X-ray absorption spectroscopy was measured at the Fe L_3-edge for $KFeF_3$ in its pristine state and after the anodic process in the cell against Li metal. Measurements at the Fe L-edge are very sensitive to changes in valence electronic structure since the 2p excitation probes the Fe 3d states, which are directly involved in the redox reactions in batteries.[52] The fluorescence yield (50 nm probing depth) of the Fe L_3-edge for $KFeF_3$ at different states of charge is shown in Figure 2b. The

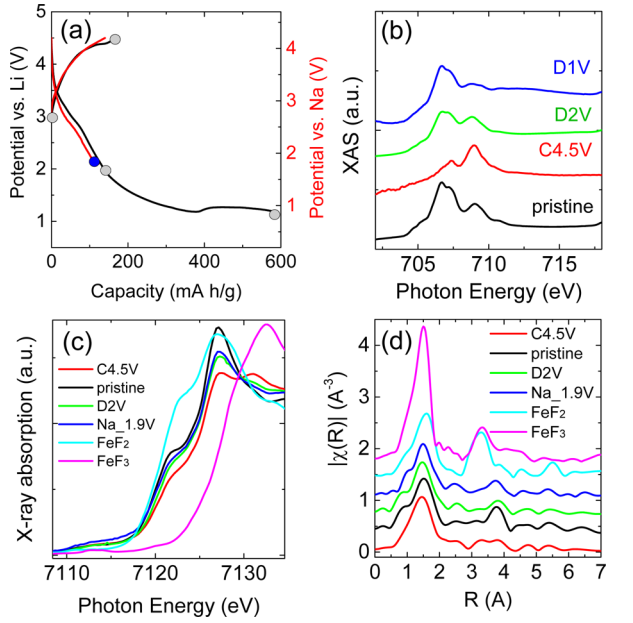

Figure 2. (a) Representative first cycle profile of $A_xK_{1-x}FeF_3$ (A = Li (black), Na (red)). Circles designate samples at different charge/discharge states chosen for XAS study, (b) XAS of Fe L-edge of $KFeF_3$ cycled versus Li at different states of charge. (c) XANES (d) and the k^2 extracted EXAFS of the Fe K-edge of $A_xK_{1-x}FeF_3$ (A = Li, Na) samples compared with FeF_2 and FeF_3. The solid curves are experimental data, and open circles are fittings.

pristine state showed an intense feature at 706, accompanied by a second one at 709 eV, which is associated with Fe^{2+}.[53] The intensity ratios of the multiplets are sensitive to changes in the iron oxidation states.[54] The two broad peaks around 706 and 709 eV reversed their intensities in the spectrum of when going from the pristine sample compared to the charged state, indicating a transition from Fe^{2+} to Fe^{3+}, with incomplete oxidation.[53] The interference of the tail of the F K-edge (696 eV) in the region of the Fe L edge (707 eV) is responsible for a complex background that hindered accurate quantification. Additional information was collected at the Fe K-edge, where changes in oxidation can be clearly observed in the form of

DOI: 10.1021/acs.chemmater.6b04181
Chem. Mater. 2017, 29, 1561−1568

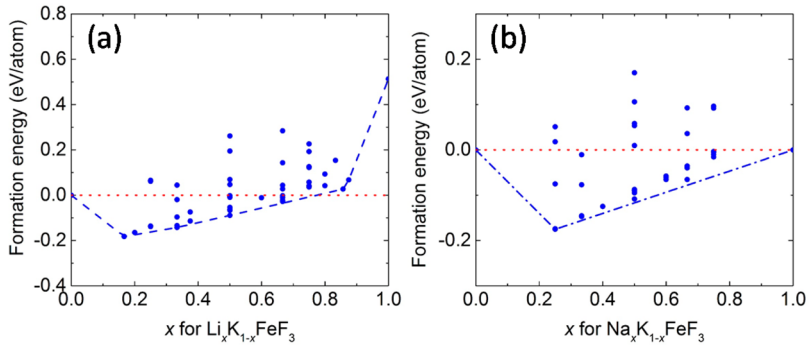

Figure 3. Formation energy of (a) $Li_xK_{1-x}FeF_3$ and (b) $Na_xK_{1-x}FeF_3$ in a perovskite framework. Each point represents one composition at a particular ordering structure. The relaxed structures with the lowest energy at each calculated composition were connected by dashed lines. The positive formation energies of $Li_xK_{1-x}FeF_3$ when x is close to 1 indicate the perovskite framework is unstable at these compositions.

solid shifts of the absorption white line, above 7115 eV for $KFeF_3$ (Figure 2c). A small pre-edge feature can be observed in the spectra of both the materials in the pristine and oxidized state due to the slightly distorted FeF_6 octahedra in the structures. The absorption edge (white line) shifted slightly to higher energy after the anodic scan to 4.5 V versus Li^+/Li^0. This state was found to be located between reference spectra of FeF_2 and FeF_3, indicating that mixtures of Fe^{2+}/Fe^{3+} were present, as expected from the electrochemistry results and consistent with the L-edge data. Above the absorption edge, the extended X-ray absorption fine structure (EXAFS) region can be analyzed in the form of a radial distribution function through a Fourier transform step. The resulting functions are shown in Figures 2d and S1, with results from fits of the data summarized in Table S1. The similarity in the observed features indicates that the structural changes are small despite the significant change in oxidation state of Fe, as would be expected from a topotactic process of deintercalation of K^+. The first peak, corresponding to Fe−F bond distances, shifted from 2.05(1) to 2.01(1) Å after the anodic scan on $KFeF_3$ in a Li metal cell. This observation is consistent with the increase in oxidation state of Fe, which should lead to shorter Fe−F bonds. The values are in line with reported Fe−F bond distances in Fe(III) and Fe(II) fluorides such as FeF_3 (Table S1).[5,27,55]

After the oxidation step, the polarization of the electrochemical cells was reversed to induce cathodic reactions (cell discharge). The resulting electrochemical profile showed hysteresis with respect to the anodic step (Figure 2a). The potential during the cathodic scan continuously decreased, with the exception of a small inflection point at ∼2.8 and 2.5 V versus Li^+/Li^0 and Na^+/Na^0, respectively. Despite this hysteresis in potential, the specific capacity during charge of the cell was highly reversible upon discharge. While the cell containing Na metal was stopped at 1.9 V versus Na^+/Na^0, for a total accumulated capacity of roughly 100 mAh/g, the electrode cycled against Li metal was further reduced to 1.0 V versus Li^+/Li^0. The result was a plateau of potential at ∼1.2 V versus Li^+/Li^0, accompanied by a large accumulated specific capacity of almost 600 mAh/g. Fe L_3-edge spectra were collected for electrodes stopped at either 2.0 or 1.0 V versus Li^+/Li^0 (Figure 2b). The spectrum of the electrode discharged to 2.0 V was consistent with the reduction of Fe^{3+} back to Fe^{2+}. Comparison with the pristine state revealed that this reduction was not complete. The center of gravity of the spectrum from a sample collected at 1.0 V was shifted to a lower energy than that of $KFeF_3$, and the multiplet at higher energy was significantly reduced, which indicated that Fe was reduced beyond the 2+ state. Thus, the process at 1.2 V versus Li^+/Li^0 corresponds to the partial conversion to Fe metal, and the destruction of the initial structure, consistent with the very large specific capacity associated with it. Because conversion reactions typically present challenges of reversibility and severe hysteresis,[16,56] and due to our fundamental interest in intercalation reactions in these fluorides, further data, discussion, and analysis of this partial conversion to metal are left outside of this study. Comparison of the Fe K-edge spectra at 2.0 V versus Li^+/Li^0 with the pristine and oxidized samples revealed a shift back toward Fe^{2+} after the cathodic step (Figure 2c), consistent with the Fe L_3-edge data. The Fe K-edge data also indicated that this reduction was not complete. For comparison purposes, the Fe K-edge spectrum of a sample recovered from a Na cell at 1.9 V versus Na^+/Na^0 was also collected. The similar signals of the samples harvested at similar potentials prove that Fe can also be reduced in the presence of either Li^+ and Na^+. Analysis of the EXAFS data (Figure 2d) revealed a very small change of bond lengths in samples at different Fe oxidation states.

The results presented so far indicate that K^+ ions are topotactically removed from $KFeF_3$ to compensate for the partial oxidation of Fe^{2+} during the cell charge. Since the electrochemical cells are rich in Li^+ or Na^+ ions, subsequent reduction must be accompanied by the intercalation of these ions into the perovskite framework to form $A_xK_yFeF_3$ (A = Li, Na). Given that these two reactions are different, irrespective of intercalated cation, it is not surprising that hysteresis exists in the electrochemical profile of the anodic and cathodic scan. These results are reminiscent of what was recently reported for $KFeSO_4F$[57] and highlight the chemical flexibility that perovskite structure can accommodate. It also emphasizes the value of electrochemical intercalation reactions as a means to discover new phases; indeed, $A_xK_yFeF_3$ phases have never been reported. First-principles calculations were performed to investigate their stability. Figure 3 shows the formation energy of perovskite structures with different K−Li and K−Na orderings. The formation energy was defined as in eq 1, where A is Li or Na:

$$E_F(K_{1-x}A_xFeF_3) = E(K_{1-x}A_xFeF_3) - (1-x)E(KFeF_3) - xE(AFeF_3) \quad (1)$$

The total energies of perovskite structures for $KFeF_3$ and $NaFeF_3$ were used.[25] Because $LiFeF_3$ is not stable when crystallizing in a perovskite framework, the structure with the lowest predicted energy ($Cmc2_1$, not perovskite structure, where layers of corner- and edge-sharing interconnected $[FeF_6]$

DOI: 10.1021/acs.chemmater.6b04181
Chem. Mater. 2017, 29, 1561−1568

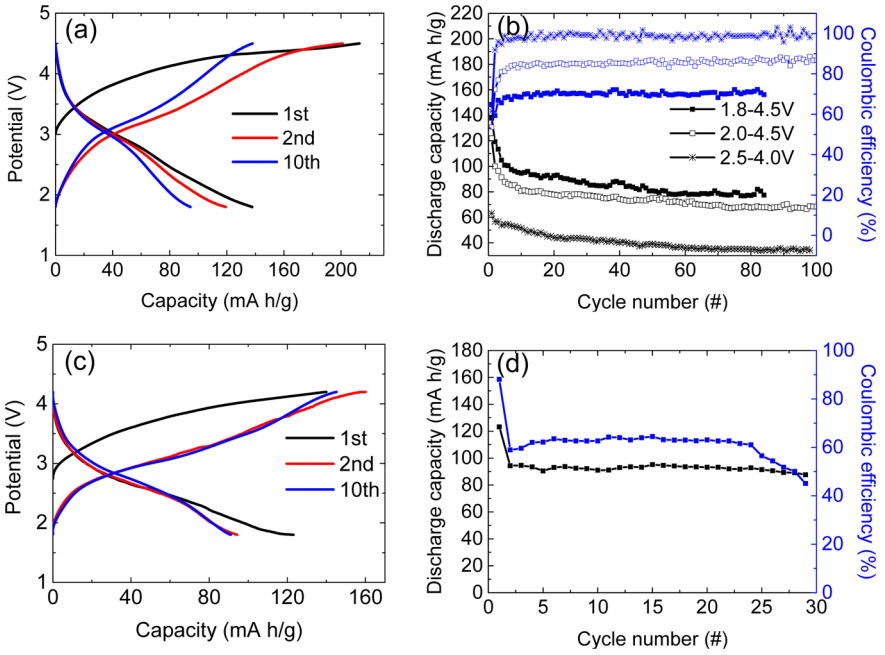

Figure 4. (a) Charge−discharge profiles of a Li/$Li_xK_{1-x}FeF_3$ cell and (b) discharge capacities and Coulombic efficiencies as a function of cycle number using different voltage windows at C/30. (c) Charge−discharge profiles of a Na/$Na_xK_{1-x}FeF_3$ cell and (d) discharge capacities and Coulombic efficiencies as a function of cycle number between 1.8 and 4.2 V at C/30.

octahedra and lithium layers arranged in an alternate fashion in an orthorhombic structure) was taken from the Materials Project (www.materialsproject.org) as a reference.[25] Here, a negative formation energy indicates the binary K−Li (or K−Na) ordering in a perovskite framework is stable against decomposing into two separate phases, $KFeF_3$ and $LiFeF_3$ (or $NaFeF_3$). As shown in Figure 3, different orderings of K−Li (or K−Na) at certain compositions give different formation energies, and the most stable orderings (lowest formation energies) at selected compositions are shown with a solid curve. The perovskite framework appears to have configurations that are stable for the whole composition range for $Na_xK_{1-x}FeF_3$ (formation energies lower than 0 eV/atom). However, the perovskite $Li_xK_{1-x}FeF_3$ phase is only stable up to about 80% Li, due to the energetically unstable cubic perovskite $LiFeF_3$ phase.[58] In conclusion, density functional theory calculations illustrate that certain perovskite compositions, $A_xK_{1-x}FeF_3$ (A = Li, Na) are thermodynamically stable against decomposition into $KFeF_3$ and $LiFeF_3$ or $NaFeF_3$, which is in agreement with our experimental results. These results also indicate that while full substitution of K^+ by Na^+ may be possible, leading to very high specific capacity, the substitution of 80% K^+ by Li^+, as quantified from the experimental electrochemical data above, may well correspond to the stability limit of the framework.

Once $A_xK_{1-x}FeF_3$ (A = Li, Na) is formed in the working electrode, it can be cycled against either Li or Na metal in a highly reversible manner. The specific charge and discharge capacity curves of the electrochemical cells at selected cycles are shown in Figure 4a and c for Li and Na, respectively. It can be readily observed that the second oxidation occurred with minimal potential hysteresis with respect to the first reduction. This chemical reversibility extended to a significant number of cycles. The observation indicates that the reaction pathways during charge and discharge are essentially the same after the first cycle so that K^+ ions were removed in the first oxidation, but either Li^+ or Na^+ ions were inserted and extracted thereafter. Indeed, evidence of both K and Na was found in a carefully rinsed electrode recovered from a Na metal cell after 10 cycles based on a combination of SEM and energy dispersive X-ray analysis (Figure S2).

Operando XRD characterization was carried out to further study the structural changes during these electrochemical reactions. Focus was placed on $KFeF_3$ in a cell with a Li metal counter electrode (and an electrolyte containing a high concentration of Li^+ ions). The XRD patterns were collected for the first oxidation−reduction cycle as well as a second oxidation. The full patterns are shown in Figure S3, with zooms in the region of the (110) and (200) reflections shown in Figure 5a and b. Two major changes were observed during

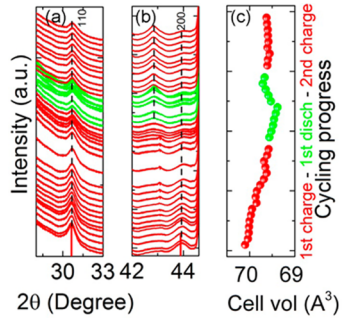

Figure 5. Operando XRD of the 1st cycle and 2nd charge process at the region of (a) (110) and (b) (200), and (c) unit cell volume change calculated from XRD.

cycling: (i) the intensity of the initial $KFeF_3$ significantly decreased, with no obvious peak shifts; (ii) a new peak appeared during the first discharge. The unit cell volumetric changes of the perovskite lattice upon cycling calculated from XRD patterns are given in Figure 5c. The unit cell volume decreased continuously (within 1% change) during the first charge as K^+ ions were removed. Relatively little change was

DOI: 10.1021/acs.chemmater.6b04181
Chem. Mater. 2017, 29, 1561−1568

observed during the subsequent Li^+ intercalation/deintercalation processes, with the exception of an apparent change in trend during the first intercalation, which could be due to a structural relaxation of $Li_yK_{1-x}FeF_3$ (where, ideally, $x = y$ at full reduction), once a critical y was achieved. The overall volume change was less than 1% on cycling. It is worthwhile noting that low values of expansion are favorable in battery electrode materials as this reduces mechanical degradation of the electrode due to the buildup of strain. These results indicate that further exploration of perovskite frameworks in search for viable electrode materials may yield phases with interesting electrochemical properties. The perovskite structure is attractive as it provides 3D channels for ions diffusion, and the original K sites should give more freedom to Li and Na ions to move.[59]

This report also provides the first evidence that Fe^{2+} and Li^+ may coexist in a perovskite framework, an interesting observation from the perspective of solid-state chemistry. While it is known that perovskite $NaFeF_3$ has a monoclinic structure due to the distortion introduced by replacing large K^+ ions (138 pm) with significantly smaller cations, Na^+ (102 pm),[60] $LiFeF_3$ has never been successfully synthesized. Interestingly, when stabilized by remaining K^+ ions, a structure close to the pristine $KFeF_3$ is retained for the partially lithiated materials. Nonetheless, an intensity decrease was observed in the (110) reflection during the initial K^+ removal, consistent with it showing the highest density of these cations in the perovskite structure. The subsequent insertion of low-Z Li^+ ions into the structure is expected to result in a sustained reduced intensity for this reflection. A simple powder XRD simulation of a hypothetical $Li_{0.5}K_{0.5}FeF_3$ composition confirmed this qualitatively (Figure S4).[51] In the operando experiments, one new reflection appeared to the left of the (200) peak, at around $2\theta = 43°$, during the first reduction. The appearance of the new XRD peak is indicative of the lower symmetry of $Li_xK_yFeF_3$, possibly introduced by ordering of K−Li ions or polyhedral distortions known to commonly occur in the perovskite crystal structures.[41,59,61] To evaluate this hypothesis, the XRD patterns of all other relaxed $Li_xK_{1-x}FeF_3$ structures from DFT calculations were simulated. The simulated XRD patterns reflect the structural changes from the Li replacement of K sites. The new peak in Figure 5b matches the strongest peak of the lowest energy structure of $Li_{1/6}K_{5/6}FeF_3$ shown in Figure S5. The ordering of Li/K in the structure introduces degeneracy within the perovskite framework and seems to be stable during early charge/recharge processes of $Li_xK_{1-x}FeF_3$. The mild inversion of the volume change of $Li_xK_yFeF_3$ during this first intercalation of Li^+ noted above would be in line with the ordering of K−Li ions.

Despite the small volume changes during the electrochemical reaction, there was a noticeable capacity loss during the first few cycles in the Li metal cells (Figure 4b), indicating a few formation cycles are required to reach equilibrium. In contrast, Na metal cells reached a stable cycling performance after the second cycle (Figure 4d); the retention between this cycle and cycle 30 was 95%, compared to 72% for the material in a Li cell. The origin of this different behavior is not clear at this point, although the higher stability of $Na_xK_{1-x}FeF_3$ compared to $Li_xK_{1-x}FeF_3$, as reflected in the calculated formation energies in Figure 3, could play a role. The Coulombic efficiencies of the cells was also well below 100% when broad potential windows were used (Figure 4b,d). This behavior indicates that the capacities during oxidation (charge) were systematically higher than upon reduction (discharge), probably due to the decomposition of electrolyte components at high potential.[62] Nonetheless, the specific capacities stabilized at a respectable ~80 mAh/g and ~90 mAh/g for Li and Na metal cells, respectively, and were sustainable for tens of cycles. As expected, the inefficiencies were reduced when a smaller voltage window was observed, but this came at the expense of lower specific capacities. For instance, when using a window of 2.5−4.0 V, the Coulombic efficiency stabilized around 100% with a capacity around 40 mAh/g. Optimization of the electrode performance was beyond the scope of this work and was not attempted.

CONCLUSIONS

In the present study, we have synthesized the parent perovskite $KFeF_3$ through a solid-state chemistry method, and material demonstrated the existence of reversible intercalation chemistry of Li or Na in a K-stabilized Fe−F perovskite framework. XAS at the Fe L_3 edge, and XANES and EXAFS at the Fe K-edge probed the $Fe^{2+/3+}$ redox chemistry in $A_xK_{1-x}FeF_3$ (A = Li, Na). Similar local chemical environments and bond lengths of $A_xK_{1-x}FeF_3$ samples observed at various states of charge collectively substantiate a mechanism of topotactic intercalation. In the case of the reaction with Li, operando XRD demonstrated the perovskite structure retention upon intercalation/extraction, the small volume change being in line with the EXAFS fitting results. DFT calculations suggest that both $Li_xK_{1-x}FeF_3$ and $Na_xK_{1-x}FeF_3$ have a relatively broad stable range of compositions crystallizing in the perovskite structure, in agreement with the experimental results. The electrochemical study on $A_xK_{1-x}FeF_3$ (A = Li, Na) illustrates this new $Fe^{2+/3+}$ redox chemistry. Moving forward, hypothetically, if phases with high Li contents could be made directly, as opposed to through extraction of K^+ in an electrochemical cell, even higher specific capacities could be achieved considering the high theoretical capacity of $LiFeF_3$ (223 mAh/g) and $NaFeF_3$ (197 mAh/g). Reducing the particle size can help to alleviate the poor conductivity of fluorides, and, consequently, improve the electrochemical performance. These prospects create opportunities for the design of a new family of attractive electrode materials.

ASSOCIATED CONTENT

Supporting Information

The Supporting Information is available free of charge on the ACS Publications website at DOI: 10.1021/acs.chemmater.6b04181.

Additional EXAFS results, SEM, EDX, XRD (PDF)

AUTHOR INFORMATION

Corresponding Author

*E-mail: jcabana@uic.edu.

ORCID

Feng Lin: 0000-0002-3729-3148

Jordi Cabana: 0000-0002-2353-5986

Present Address

‖Department of Chemistry, Virginia Tech, Blacksburg, Virginia 24061, United States.

Notes

The authors declare no competing financial interest.

DOI: 10.1021/acs.chemmater.6b04181
Chem. Mater. 2017, 29, 1561−1568

■ ACKNOWLEDGMENTS

Work at Lawrence Berkeley National Laboratory was supported by the Assistant Secretary for Energy Efficiency and Renewable Energy, Office of Vehicle Technologies of the U.S. Department of Energy (DOE) under Contract No. DE-AC02-05CH11231, as part of the Battery Materials Research (BMR) Program. M.R.P. and J.C. acknowledge research start-up funding by the Department of Chemistry and the College of Liberal Arts and Sciences at the University of Illinois at Chicago. Portions of this research were carried out at the Stanford Synchrotron Radiation Lightsource, a Directorate of SLAC National Accelerator Laboratory and an Office of Science User Facility operated for the U.S. Department of Energy Office of Science by Stanford University. Beamline 20-BM at the Advanced Photon Source (APS) is part of the Pacific Northwest Consortium-X-ray Science Division (PNC/XSD) facilities, supported by the U.S. DOE Office of Science, the Canadian Light Source (CLS), and its funding partners, the University of Washington and the APS. Use of the APS, an Office of Science User Facility operated for the DOE by Argonne National Laboratory, was supported by Contract No. DE-AC02-06CH11357.

■ REFERENCES

(1) Van Noorden, R. The Rechargable Revolution: A Better Battery. *Nature* **2014**, *507*, 26−28.

(2) Ma, Y.; Lockwood, G. K.; Garofalini, S. H. Development of a Transferable Variable Charge Potential for the Study of Energy Conversion Materials FeF_2 and FeF_3. *J. Phys. Chem. C* **2011**, *115*, 24198−24205.

(3) Kim, S.-W.; Nam, K.-W.; Seo, D.-H.; Hong, J.; Kim, H.; Gwon, H.; Kang, K. Energy Storage in Composites of a Redox Couple Host and a Lithium Ion Host. *Nano Today* **2012**, *7*, 168−173.

(4) Tan, H. J.; Smith, H. L.; Kim, L.; Harding, T. K.; Jones, S. C.; Fultz, B. Electrochemical Cycling and Lithium Insertion in Nanostructured FeF_3 Cathodes. *J. Electrochem. Soc.* **2014**, *161*, A445−A449.

(5) Li, C.; Yin, C.; Gu, L.; Dinnebier, R. E.; Mu, X.; van Aken, P. A.; Maier, J. An $FeF_3{\cdot}0.5H_2O$ Polytype: A Microporous Framework Compound with Intersecting Tunnels for Li and Na Batteries. *J. Am. Chem. Soc.* **2013**, *135*, 11425−11428.

(6) Liu, J.; Wan, Y.; Liu, W.; Ma, Z.; Ji, S.; Wang, J.; Zhou, Y.; Hodgson, P.; Li, Y. Mild and Cost-Effective Synthesis of Iron Fluoride-Graphene Nanocomposites for High-Rate Li-ion Battery Cathodes. *J. Mater. Chem. A* **2013**, *1*, 1969−1975.

(7) Li, C.; Gu, L.; Tsukimoto, S.; van Aken, P. A.; Maier, J. Low-Temperature Ionic-Liquid-Based Synthesis of Nanostructured Iron-Based Fluoride Cathodes for Lithium Batteries. *Adv. Mater.* **2010**, *22*, 3650−3654.

(8) Wiaderek, K. M.; Borkiewicz, O. J.; Castillo-Martínez, E.; Robert, R.; Pereira, N.; Amatucci, G. G.; Grey, C. P.; Chupas, P. J.; Chapman, K. W. Comprehensive Insights into the Structural and Chemical Changes in Mixed-Anion FeOF Electrodes by Using Operando PDF and NMR Spectroscopy. *J. Am. Chem. Soc.* **2013**, *135*, 4070−4078.

(9) Recham, N.; Rousse, G.; Sougrati, M. T.; Chotard, J.-N.; Frayret, C.; Mariyappan, S.; Melot, B. C.; Jumas, J.-C.; Tarascon, J.-M. Preparation and Characterization of a Stable $FeSO_4F$-based Framework for Alkali Ion Insertion Electrodes. *Chem. Mater.* **2012**, *24*, 4363.

(10) Sobkowiak, A.; Roberts, M.; Häggström, L.; Ericsson, T.; Andersson, A. M.; Edstrom, K.; Gustafsson, T.; Björefors, F. G. Identification of an Intermediate Phase, $Li_{1/2}FeSO_4F$, Formed During Electrochemical Cycling of Tavorite $LiFeSO_4F$. *Chem. Mater.* **2014**, *26*, 4620.

(11) Badway, F.; Cosandey, F.; Pereira, N.; Amatucci, G. G. Carbon Metal Fluoride Nanocomposites - High-Capacity Reversible Metal Fluoride Conversion Materials as Rechargeable Positive Electrodes for Li Batteries. *J. Electrochem. Soc.* **2003**, *150*, A1318−A1327.

(12) Kim, S.-W.; Seo, D.-H.; Gwon, H.; Kim, J.; Kang, K. Fabrication of FeF_3 Nanoflowers on CNT Branches and Their Application to High Power Lithium Rechargeable Batteries. *Adv. Mater.* **2010**, *22*, 5260−5264.

(13) Amatucci, G. G.; Pereira, N. Fluoride Based Electrode Materials for Advanced Energy Storage Devices. *J. Fluorine Chem.* **2007**, *128*, 243−262.

(14) Wang, F.; Robert, R.; Chernova, N. A.; Pereira, N.; Omenya, F.; Badway, F.; Hua, X.; Ruotolo, M.; Zhang, R.; Wu, L.; Volkov, V.; Su, D.; Key, B.; Whittingham, M. S.; Grey, C. P.; Amatucci, G. G.; Zhu, Y.; Graetz, J. Conversion Reaction Mechanisms in Lithium Ion Batteries: Study of the Binary Metal Fluoride Electrodes. *J. Am. Chem. Soc.* **2011**, *133*, 18828−18836.

(15) Wang, F.; Yu, H.-C.; Chen, M.-H.; Wu, L.; Pereira, N.; Thornton, K.; Van der Ven, A.; Zhu, Y.; Amatucci, G. G.; Graetz, J. Tracking Lithium Transport and Electrochemical Reactions in Nanoparticles. *Nat. Commun.* **2012**, *3*, 1201.

(16) Cabana, J.; Monconduit, L.; Larcher, D.; Palacín, M. R. Beyond Intercalation-Based Li-Ion Batteries: The State of the Art and Challenges of Electrode Materials Reacting Through Conversion Reactions. *Adv. Mater.* **2010**, *22*, E170−E192.

(17) Whittingham, M. S. Ultimate Limits to Intercalation Reactions for Lithium Batteries. *Chem. Rev.* **2014**, *114*, 11414.

(18) Basa, A.; Gonzalo, E.; Kuhn, A.; Garcia-Alvarado, F. Reaching the Full Capacity of the Electrode Material Li_3FeF_6 by Decreaing the Particle Size to Nanoscale. *J. Power Sources* **2012**, *197*, 260−266.

(19) Gonzalo, E.; Kuhn, A.; Garcia-Alvarado, F. A Comparative Study of a- and b- Li_3FeF_6: Structure and Electrochemical Behavior. *J. Electrochem. Soc.* **2010**, *157*, A1002−A1006.

(20) Liao, P.; Li, J.; Dahn, J. R. Lithium Intercalation in $LiFe_2F_6$ and $LiMgFeF_6$ Disordered Trirutile-Type Phases. *J. Electrochem. Soc.* **2010**, *157*, A355−A361.

(21) Lieser, G.; Drager, C.; Schroeder, M.; Indris, S.; de Biasi, L.; Gesswein, H.; Glatthaar, S.; Ehrenberg, H.; Binder, J. R. Sol-Gel Based Synthesis of $LiNiFeF_6$ and Its Electrochemical Characterzation. *J. Electrochem. Soc.* **2014**, *161*, A1071−A1077.

(22) Shakoor, R. A.; Lim, S. Y.; Kim, H.; Nam, K.-W.; Kang, J. K.; Kang, K.; Choi, J. W. Mechanochemical Synthesis and Electrochemical Behavior of Na_3FeF_6 in Sodium and Lithium Batteries. *Solid State Ionics* **2012**, *218*, 35−40.

(23) Tressaud, A.; Portier, J.; de Pape, R.; Hagenmuller, P. Les Systèmes *M*F-FeF_3 (*M* = Li, Na, K, Rb, Cs, Tl, NH_4). *J. Solid State Chem.* **1970**, *2*, 269−277.

(24) Tressaud, A.; Portier, J.; Shearer-Turrell, S.; Dupin, J.-L.; Hagenmuller, P. Les Hexafluoferrites M_3FeF_6 (*M* = Li, Na, K, Rb, Cs, Ag, Tl, NH_4): Etude Radiocristallographique, Spectroscopique et Magnetique. *J. Inorg. Nucl. Chem.* **1970**, *32*, 2179−2186.

(25) Jain, A.; Ong, S. P.; Hautier, G.; Chen, W.; Richards, W. D.; Dacek, S.; Cholia, S.; Gunter, D.; Skinner, D.; Ceder, G.; Persson, K. A. Commentary: The Materials Project: A Materials Genome Approach to Accelerating Materials Innovation. *APL Mater.* **2013**, *1*, 011002.

(26) Rudowicz, C.; Piwowarska, D. Spectroscopic Properties of Fe^{2+} Ions at Tetragonal Sites-Crystal Field Effects and Microscopic Modeling of Spin Hamiltonian Parameters for Fe^{2+} (S = 2) Ions in K_2FeF_4 and K_2ZnF_4. *J. Magn. Magn. Mater.* **2011**, *323*, 2681−2689.

(27) Okazaki, A.; Suemune, Y. The Crystal Structures of $KMnF_3$, $KFeF_3$, $KCoF_3$, $KNiF_3$ and $KCuF_3$ Above and Below Their Neel Temperatures. *J. Phys. Soc. Jpn.* **1961**, *16*, 671−675.

(28) Yamada, Y.; Doi, T.; Tanaka, I.; Okada, S.; Yamaki, J.-i. Liquid-phase Synthesis of Highly Dispersed $NaFeF_3$ Particles and Their Electrochemical Properties for Sodium-ion Batteries. *J. Power Sources* **2011**, *196*, 4837−4841.

(29) Pena, M. A.; Fierro, J. L. G. Chemical Structures and Performance of Perovskite Oxides. *Chem. Rev.* **2001**, *101*, 1981−2017.

(30) Goldschmidt, V. V. M Die Gesetze der Krystallochemie. *Naturwissenschaften* **1926**, *14* (21), 477.

(31) Dimov, N.; Nishimura, A.; Chihara, K.; Kitajou, A.; Gocheva, I. D.; Okada, S. Transition Metal $NaMF_3$ Compounds as Model Systems

DOI: 10.1021/acs.chemmater.6b04181
Chem. Mater. 2017, 29, 1561−1568

for Studying the Feasibility of Ternary Li-*M*-F and Na-*M*-F Single Phases as Cathodes for Lithium−ion and Sodium−ion Batteries. *Electrochim. Acta* **2013**, *110*, 214−220.
(32) Ishihara, T.; Matsuda, H.; Takita, Y. Doped $LaGaO_3$ Perovskite Type Oxide as a New Oxide Ionic Conductor. *J. Am. Chem. Soc.* **1994**, *116*, 3801−3803.
(33) Thangadurai, V.; Shukla, A. K.; Gopalakrishnan, J. $La_{0.9}Sr_{0.1}Ga_{0.8}Mn_{0.2}O_{2.85}$: a New Oxide Ion Conductor. *Chem. Commun.* **1998**, 2647−2648.
(34) Feng, M.; Goodenough, J. B. A Superior Oxide-ion Electrolyte. *Eur. J. Solid State Inorg. Chem.* **1994**, *31*, 663−672.
(35) Steele, B. C. H.; Bae, J.-M. Properties of $La_{0.6}Sr_{0.4}Co_{0.2}Fe_{0.8}O_{3-x}$ (LSCF) Double Layer Cathodes on Gadolinium-doped Cerium Oxide (CGO) Electrolytes: II. Role of Oxygen Exchange and Diffusion. *Solid State Ionics* **1998**, *106*, 255−261.
(36) Green, M. A.; Ho-Baillie, A.; Snaith, H. J. The Emergence of Perovskite Solar Cells. *Nat. Photonics* **2014**, *8*, 506−514.
(37) Sullivan, E.; Avdeev, M.; Vogt, T. Structural Distortions in $Sr_{3-x}A_xMO_4F$ (*A*=Ca, Ba; *M*=Al, Ga, In) Anti-Perovskites and Corresponding Changes in Photoluminescence. *J. Solid State Chem.* **2012**, *194*, 297−306.
(38) Suntivich, J.; May, K. J.; Gasteiger, H. A.; Goodenough, J. B.; Shao-Horn, Y. A Perovskite Oxide Optimized for Oxygen Evolution Catalysis from Molecular Orbital Principles. *Science* **2011**, *334*, 1383−1385.
(39) Han, X.; Hu, Y.; Yang, J.; Cheng, F.; Chen, J. Porous Perovskite $CaMnO_3$ as an Electrocatalyst for Rechargeable Li-O2 Batteries. *Chem. Commun.* **2014**, *50*, 1497−1499.
(40) Takada, K. Secondary Batteries−Lithium Rechargable Systems−Lithium-ion Electrolytes: Solid Oxide. In *Encyclopedia of Electrochemical Power Sources*; Garche, J., Ed.; Elsevier: Amsterdam, 2009; pp 328−336.
(41) Wang, G. X.; Yao, P.; Bradhurst, D. H.; Dou, S. X.; Liu, H. K. Structure Characterisation and Lithium Insertion in $La_{0.33}NbO_3$ Perovskite. *Solid State Ionics* **1999**, *124*, 37−43.
(42) Doeff, M. M.; Chen, G.; Cabana, J.; Richardson, T. J.; Mehta, A.; Shirpour, M.; Duncan, H.; Kim, C.; Kam, K. C.; Conry, T. Characterization of Electrode Materials for Lithium Ion and Sodium Ion Batteries Using Synchrotron Radiation Techniques. *J. Visualized Exp.* **2013**, e50594.
(43) Ravel, B.; Newville, M. ATHENA; ARTEMIS; HEPHAESTUS, Data Analysis for *X*-ray Absorption Sepctroscopy Using IFEFFIT. *J. Synchrotron Radiat.* **2005**, *12*, 537−541.
(44) van de Walle, A.; Ceder, G. Automating First-principles Phase Diagram Calculations. *J. Phase Equilib.* **2002**, *23*, 348−359.
(45) Chen, W.; Dalach, P.; Schneider, W. F.; Wolverton, C. Interplay Between Subsurface Ordering, Surface Segregation, and Adsorption on Pt−Ti(111) Near-Surface Alloys. *Langmuir* **2012**, *28*, 4683−4693.
(46) Chen, W.; Schmidt, D.; Schneider, W. F.; Wolverton, C. First-principles Cluster Expansion Study of Missing-row Reconstructions of FCC (110) Surfaces. *Phys. Rev. B: Condens. Matter Mater. Phys.* **2011**, *83*, 075415.
(47) Kresse, G.; Joubert, D. From Uultrasoft Pseudopotentials to the Projector Augmented-wave Method. *Phys. Rev. B: Condens. Matter Mater. Phys.* **1999**, *59*, 1758−1775.
(48) Kresse, G.; Furthmüller, J. Efficient Iterative Schemes for *Ab initio* Total-energy Calculations Using a Plane-wave Basis Set. *Phys. Rev. B: Condens. Matter Mater. Phys.* **1996**, *54*, 11169−11186.
(49) Perdew, J. P.; Burke, K.; Ernzerhof, M. Generalized Gradient Approximation Made Simple. *Phys. Rev. Lett.* **1996**, *77*, 3865−3868.
(50) Jain, A.; Hautier, G.; Moore, C. J.; Ping Ong, S.; Fischer, C. C.; Mueller, T.; Persson, K. A.; Ceder, G. A High-Throughput Infrastructure for Density Functional Theory Calculations. *Comput. Mater. Sci.* **2011**, *50*, 2295−2310.
(51) Kraus, W.; Nolze, G. *PowderCell, 2.4*; Federal Institute for Materials Research and Testing: Berlin, Germany, 2000.
(52) Giorgetti, M. A Review on the Structural Studies of Batteries and Host Materials by X-Ray Absorption Spectroscopy. *ISRN Mater. Sci.* **2013**, *2013*, 938625.
(53) Liu, X.; Liu, J.; Qiao, R.; Yu, Y.; Li, H.; Suo, L.; Hu, Y.-S.; Chuang, Y.-D.; Shu, G.; Chou, F.; Weng, T.-C.; Nordlund, D.; Sokaras, D.; Wang, Y. J.; Lin, H.; Barbiellini, B.; Bansil, A.; Song, X.; Liu, Z.; Yan, S.; Liu, G.; Qiao, S.; Richardson, T. J.; Prendergast, D.; Hussain, Z.; de Groot, F. M. F.; Yang, W. Phase Transformation and Lithiation Effect on Electronic Structure of Li_xFePO_4: An In-Depth Study by Soft *X*-ray and Simulations. *J. Am. Chem. Soc.* **2012**, *134*, 13708−13715.
(54) Graetz, J.; Ahn, C. C.; Ouyang, H.; Rez, P.; Fultz, B. White Lines and *d*-band Occupancy for the 3*d* Transition-metal Oxides and Lithium Transition-metal Oxides. *Phys. Rev. B: Condens. Matter Mater. Phys.* **2004**, *69*, 235103.
(55) Knox, K. Perovskite-Like Fluorides: I. Structures of $KMnF_3$, $KFeF_3$, $KCoF_3$, $KNiF_3$ and $KZnF_3$. Crystal Field Effects in the Series and in $KCrF_3$ and $KCuF_3$. *Acta Crystallogr.* **1961**, *14*, 583.
(56) Ko, J. K.; Wiaderek, K. M.; Pereira, N.; Kinnibrugh, T. L.; Kim, J. R.; Chupas, P. J.; Chapman, K. W.; Amatucci, G. G. Transport, Phase Reactions, and Hysteresis of Iron Fluoride and Oxyfluoride Conversion Electrode Materials for Lithium Batteries. *ACS Appl. Mater. Interfaces* **2014**, *6*, 10858−10869.
(57) Yang, F.; Liu, Y.; Martha, S. K.; Wu, Z.; Andrews, J. C.; Ice, G. E.; Pianetta, P.; Nanda, J. Nanoscale Morphological and Chemical Changes of High Voltage Lithium−Manganese Rich NMC Composite Cathodes with Cycling. *Nano Lett.* **2014**, *14*, 4334−4341.
(58) Doe, R. E.; Persson, K. A.; Meng, Y. S.; Ceder, G. First-Principles Investigation of the Li−Fe−F Phase Diagram and Equilibrium and Nonequilibrium Conversion Reactions of Iron Fluorides with Lithium. *Chem. Mater.* **2008**, *20*, 5274−5283.
(59) Inoue, N.; Zou, Y. Physical Properties of Perovskite-type Lithium Ionic Conductor. *Physics of Solid State Ionics* **2006**, 247−269.
(60) Shannon, R. Revised Effective Ionic Radii and Systematic Studies of Interatomic Distances in Halides and Chalcogenides. *Acta Crystallogr., Sect. A: Cryst. Phys., Diffr., Theor. Gen. Crystallogr.* **1976**, *32*, 751−767.
(61) Gabrisch, H.; Yi, T.; Yazami, R. Transmission Electron Microscope Studies of $LiNi_{1/3}Mn_{1/3}Co_{1/3}O_2$ before and after Long-Term Aging at 70 °C. *Electrochem. Solid-State Lett.* **2008**, *11*, A119−A124.
(62) Lux, S. F.; Pollak, E.; Boesenberg, U.; Richardson, T.; Kostecki, R. Electrochemical Reactivity of Pyrolytic Carbon Film Electrodes in Organic Carbonate Electrolytes. *Electrochem. Commun.* **2014**, *46*, 5−8.

DOI: 10.1021/acs.chemmater.6b04181
Chem. Mater. 2017, 29, 1561−1568